





Authigenic clay mineral evidence for restricted, evaporitic conditions during the emergence of the Ediacaran Doushantuo Biota

Shujun Han ^{1,2✉}, Stefan C. Löhner ^{1,3}, April N. Abbott⁴, Andre Baldermann ⁵, Martin Voigt ^{6,7} & Bingsong Yu²

The Ediacaran Period witnessed major environmental change and an expansion of eukaryotic life following the Marinoan glaciation. The Doushantuo Formation of south China has furnished much of our understanding of Earth System and biosphere evolution during this period, but its depositional setting—marine or non-marine—is still debated. Here we conduct mineralogical, petrographic and geochemical analyses of samples from the lower Doushantuo Formation in order to determine the origin of saponite clay minerals which are abundant in this interval. We find that the morphology and distribution of the saponite clays suggest they are of pre-compaction, authigenic origin. We infer that the lower Doushantuo sediments were deposited in a restricted, mildly evaporitic lagoonal basin, offering additional constraints on the environmental setting into which metazoan life emerged. Further, our findings confirm that Ediacaran seawater favored reverse weathering, with marine clay formation likely representing an important sink for various elements during the Precambrian.

¹School of Natural Sciences, Macquarie University, Sydney, NSW 2109, Australia. ²School of Earth Sciences and Resources, China University of Geosciences (Beijing), Beijing 100083, China. ³Department of Earth Sciences, University of Adelaide, Adelaide, SA 5005, Australia. ⁴Department of Marine Science, Coastal Carolina University, Conway, SC 29528, USA. ⁵Institute of Applied Geosciences, Graz University of Technology, NAWI Graz Geocentre, Rechbauerstraße 12, 8010 Graz, Austria. ⁶Institute of Earth Sciences, University of Iceland, Sturlugata 7, 102 Reykjavik, Iceland. ⁷Carbfix, Bæjarháls 1, 110 Reykjavik, Iceland. ✉email: cugbhansj@126.com

The Doushantuo Formation of South China preserves a unique sedimentary record of major paleo-environmental change in the aftermath of the Marinoan glaciation¹ as well as the subsequent expansion of eukaryotic life. The lower Ediacaran Doushantuo Biota, which have been primarily recognised in shallow-water settings, include multicellular algae² and a diverse suite of acanthomorphic acritarchs³ including embryo-like fossils which are candidates for the earliest animal life on Earth^{2,4}. While the metazoan affinity of the embryo-like fossils is contested⁵, it is nevertheless widely accepted that the Doushantuo Formation provides an important record of the environmental setting and nature of eukaryotic expansion during the interval in time that metazoans first diversified⁶. In this context, the disputed marine versus non-marine nature of the shallow-water, fossil-bearing deposits of the basal Doushantuo Formation^{7,8} represents an important knowledge gap in our understanding of the environmental controls on the emergence of early life.

Current stratigraphic and paleo-geographic models of the Yangtze Block suggest that the Doushantuo Formation was deposited on a passive continental margin spanning tidal flat–shelf lagoon settings in the North West (Yichang City) to basinal settings in the South East (northern Guangxi Province, Fig. 1)⁹. An expanded sedimentary record amenable to geochemical characterisation, together with an abundant and diverse fossil record, have made the shallow-water sequences of the Yangtze Gorges Area (YGA) in particular a key locality for geobiological and paleo-environmental studies and the epicenter of the debate over the environmental setting into which the Doushantuo Biota emerged. The Doushantuo Formation in the YGA is commonly divided into four lithostratigraphic members^{9,10}: the 1st member consists of cap carbonates that sharply overlie the glacial diamictite of the Nantuo Formation; the 2nd member comprises interbedded shale and dolostone with

chert and phosphatic nodules, with abundant saponite throughout; the 3rd member is made up of dolostone and bedded chert in the lower part and ribbon rocks in the upper part; the 4th member consists of black shale characterized by highly illitic mixed-layered illite/smectite and discrete illite, but no saponite⁷. This sedimentary sequence is overlain by the upper Ediacaran Dengying Formation⁹.

Clay minerals are persuasive paleo-environmental indicators, provided that the origin and mode of formation of the clay can be unambiguously identified¹¹. The presence of saponite, a Mg-rich, trioctahedral 2:1 clay mineral of the smectite group, in the 2nd member of the Doushantuo Formation has been central to the debate over the sedimentary setting of the YGA^{7,8}. Saponite is known to form by various mechanisms, including (1) hydrothermal alteration of (ultra)mafic igneous rocks, volcanic ash or siliceous dolostone^{12–15}; (2) transformation of clay minerals (e.g. nontronite-saponite series transformation under hydrothermal conditions¹⁶, or talc-saponite in submarine hydrothermal settings¹⁷); (3) pedogenic weathering of (ultra)mafic silicates under humid conditions¹⁸; (4) precipitation from gel precursors under alkaline conditions¹⁹ or (5) direct precipitation from supersaturated solutions (including pore fluids)^{20,21}. Crucially, although saponite can potentially form in both marine and non-marine settings, abundant syn-depositional saponite precipitation in open marine or shelf settings has not been documented. Local accumulations of detrital pedogenic saponites are, in principle, possible, but in the Phanerozoic, a marine origin is typically restricted to the alteration of volcanic ash layers under reducing conditions or to hydrothermal systems¹⁵. In contrast, saponite formation in alkaline or evaporitic lakes is common and well documented^{11,19,22,23}. We note, however, that reverse weathering may have been a more important feature of the Si-rich Proterozoic oceans²⁴, meaning that marine clay authigenesis (including

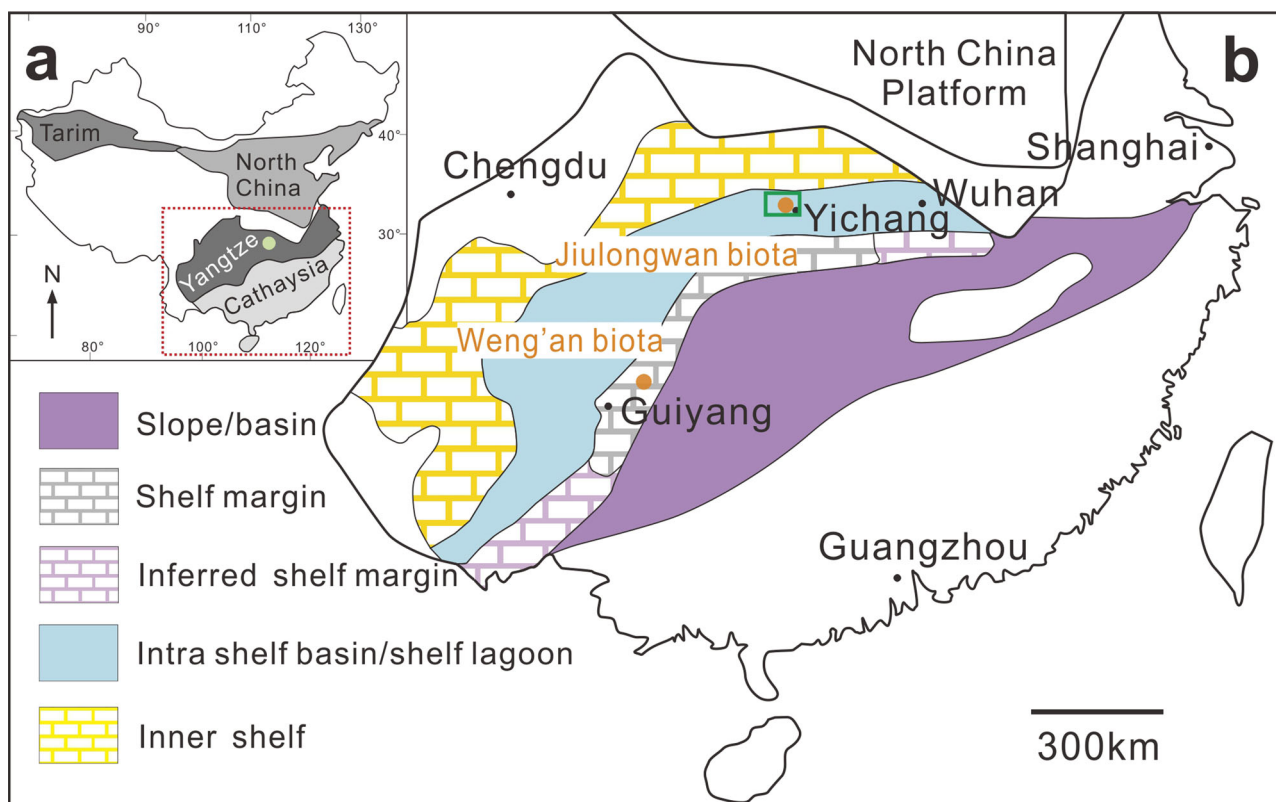


Fig. 1 Geological map of the Yangtze Gorges Area. a Location of the Yangtze Block **(b)** Location and generalized paleogeographic reconstruction of the Yangtze platform during Doushantuo deposition (adapted from ref. ⁹) and locations of the investigated Sixi Section and Qinglinkou Section (green rectangle).

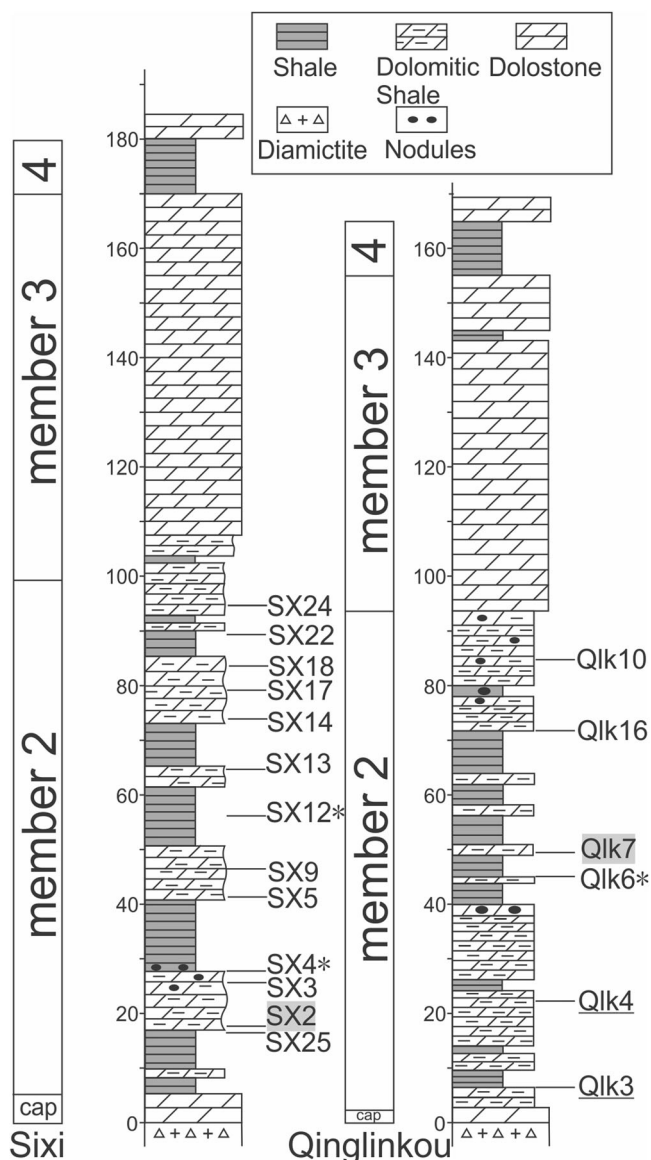


Fig. 2 Lithological logs of the Sixi Section and Qinglinkou Section with sample positions shown. Two representative samples chosen for EPMA are denoted in grey shade; Asterisk denotes samples containing potential phosphatic fossils. Underlined samples have unusual petrographic features and are not further considered for the present study: Qlk3 comprises laminated illite and quartz and Qlk4 is completely chloritized.

saponite) was potentially more widespread in the Precambrian. This latter possibility remains largely untested because of the difficulty of distinguishing and quantifying clay minerals of authigenic versus detrital origin.

The spatial distribution of saponite offers clues as to its origin. The 2nd member in the YGA contains abundant saponite, whereas equivalent sequences in open marine slope to basin settings do not⁷. Initially, this was interpreted as evidence that the lower Doushantuo Formation in the YGA was deposited in an alkaline lake setting disconnected from the ocean⁷. Subsequent work, in contrast, inferred an open marine setting for the YGA arguing that the saponite was likely of detrital terrestrial weathering origin and thus not indicative of the depositional environment⁸. However, this study did not identify or characterise the clay mineral assemblage, relying instead on indirect constraints including bulk geochemical data for the 2nd member

consistent with a mafic-ultramafic provenance⁸. The presence and origin of saponite in these sections remains unresolved despite major implications for determining the marine versus non-marine origin of the Doushantuo Biota, informing the interpretation of isotope proxy records^{25–27}, and testing recent models invoking widespread marine clay authigenesis in the Precambrian Ocean²⁴.

A fundamental limitation of previous studies is their reliance on bulk mineralogical and indirect geochemical techniques, which are unable to differentiate saponite of detrital origin from saponite of authigenic origin. Recent technical and methodological advances in scanning electron microscope - energy dispersive spectroscopy (SEM-EDS) based petrography now allow the differentiation and quantification of clays of distinct genetic origins^{28,29}. Here we couple this petrographic approach with X-ray diffraction (XRD) techniques and electron probe microanalysis (EPMA) to conclusively identify saponite mode of formation in 19 samples collected from the Doushantuo 2nd Member in two representative sections of the YGA (Fig. 2). This provides previously unobtainable constraints on the depositional setting associated with the emergence of the Doushantuo Biota, and demonstrates a robust approach with which to identify authigenic clays and test the prevalence of reverse weathering in the Precambrian²⁴.

Results and discussion

Quantitative SEM-EDS mineral mapping shows that the dolomitic shales and dolostones in the 2nd member of the Doushantuo Formation mainly consist of dolomite (16.9–75.3 wt%), quartz (3.8–40.6 wt%), feldspar (0–33.1 wt%), and clay minerals (4.3–34.4 wt%), excluding an unusual illite-dominated sample (Qlk3) and a heavily altered sample (Qlk6*) close to the cap carbonate in the Qinglinkou section (Table 1, Fig. 2). Mineral mapping identifies saponite, chlorite and muscovite as the most common phyllosilicates (Table 1). Consistent with this, XRD analysis of Ca-saturated, oriented clay preparations identifies a dominance of mixed-layered chlorite/smectite with (001) peak located between 1.40 nm and 1.48 nm (air-dried), expanding to between 1.52 and 1.66 nm after ethylene glycol solvation and then collapsing to ~1.40 nm and ~1.00 nm on heating to 400 °C (Fig. 3a) and minor illite/mica ((001) reflection at 1.0 nm). We attribute variable (001) peak positions to varying proportions of smectite in the irregular mixed-layered chlorite/smectite (R0) of different samples. The (002) peaks (0.76–0.83 nm) in ethylene glycol solvated samples suggest a smectite proportion between 40% and 80%³⁰. The smectite clay fraction is confirmed as saponite by powder XRD analysis of the <2 μm fraction showing the (060) peak located between 0.154 nm and 0.153 nm (Fig. 3b), demonstrating the trioctahedral nature of the clay³¹, as well as EPMA showing high magnesium content (~23 wt% MgO; Supplementary Fig. 2, Supplementary Data 2) and lower values of aluminum (~10 wt% Al₂O₃) and iron (~3 wt% FeO), typical of saponite²². The average formula of saponite calculated from EPMA results is (K_{0.19}Ca_{0.07})(Mg_{2.63}Fe_{0.20}Al_{0.34})[Si_{3.35}Al_{0.61}O₁₀](OH)₂.

Saponite dominates the clay fraction (70.0 wt%, on average) (Fig. 4a), followed by chlorite (25.7 wt% on average), whereas muscovite contributes only 4.3 wt% on average. Saponite is concentrated in bedding-parallel laminae up to 120 μm in length and 5–10 μm thick (Fig. 4b) or in intergranular pore-fill domains (Fig. 4d, f). It also occurs, more rarely, as intragranular pore-fill in feldspar (Fig. 4g). Saponite is commonly partially altered to and intergrown with chlorite, but retains the morphology of surrounding unaltered saponite (Fig. 4b, d). Saponite domains contain negligible amounts of detrital material and exhibit

Table 1 Mineralogical composition of the Doushantuo samples derived from SEM-EDS mineral mapping (FEI Nanomin/Maps Mineralogy).

| mineral/ sample | Quartz (wt %) | Alkali Feldspar (wt%) | Plagioclase (wt %) | Muscovite (wt %) | Illite ^a (wt %) | Chlorite (wt %) | Smectite (wt %) | Calcite (wt %) | Dolomite (wt %) | Ankerite (wt %) | Apatite (wt %) | Pyrite (wt %) | Note |
|--------------------|------------------|--------------------------|-----------------------|---------------------|-------------------------------|--------------------|--------------------|-------------------|--------------------|--------------------|-------------------|------------------|---------|
| SX25 | 27.3 | 3.5 | 5.8 | 0.2 | <0.1 | 2.8 | 12.5 | 10.1 | 32.1 | 1.3 | 0.3 | 3.8 | |
| SX2 ROI1 | 15.2 | 9.5 | 8.5 | 1.7 | <0.1 | <0.1 | 18.0 | <0.1 | 39.2 | 4.4 | 0.9 | 2.1 | |
| SX2 ROI2 | 16.4 | 11.6 | 9.1 | 1.7 | <0.1 | <0.1 | 17.6 | <0.1 | 35.0 | 3.8 | 1.2 | 3.5 | |
| SX3 | 14.6 | 1.0 | 1.2 | 0.3 | <0.1 | 3.9 | 8.8 | <0.1 | 65.9 | 3.1 | 0.2 | 0.9 | |
| SX4 | 25.0 | 5.1 | 5.5 | 0.2 | <0.1 | 1.9 | 3.2 | <0.1 | 47.5 | 2.0 | 7.6 | 1.8 | |
| SX5 | 31.9 | 9.6 | 8.6 | 0.3 | <0.1 | 3.6 | 3.4 | <0.1 | 35.0 | 2.1 | 2.6 | 2.4 | |
| SX9 ROI1 | 19.5 | 2.0 | 2.5 | 0.5 | <0.1 | 8.5 | 8.8 | <0.1 | 52.0 | 3.5 | 0.9 | 1.6 | |
| SX9 ROI2 | 25.6 | 3.0 | 2.9 | <0.1 | <0.1 | <0.1 | 13.8 | <0.1 | 49.1 | 3.2 | 0.7 | 1.6 | |
| SX12 | 19.8 | 8.6 | 8.4 | 0.4 | <0.1 | 5.1 | 8.2 | <0.1 | 41.1 | 2.3 | 2.7 | 3.1 | |
| SX13 | 12.1 | <0.1 | <0.1 | <0.1 | <0.1 | 1.9 | 4.0 | <0.1 | 75.3 | 2.3 | 0.3 | 4.1 | |
| SX14 | 3.8 | 0.7 | 0.8 | 0.1 | <0.1 | 0.6 | 16.7 | <0.1 | 72.2 | 2.4 | 1.8 | 0.8 | |
| SX17 | 15.4 | 2.2 | 2.1 | 0.1 | <0.1 | 1.6 | 13.8 | <0.1 | 56.7 | 1.1 | 5.5 | 1.4 | |
| SX18 | 10.7 | 7.7 | 4.0 | 1.7 | <0.1 | 6.1 | 22.2 | <0.1 | 41.0 | 2.7 | 1.7 | 2.1 | |
| SX22 ROI1 | 7.9 | 11.4 | 4.3 | 2.1 | <0.1 | <0.1 | 31.3 | <0.1 | 34.5 | 2.1 | 3.6 | 2.4 | |
| SX22 ROI2 | 6.7 | <0.1 | 3.5 | 2.2 | <0.1 | <0.1 | 32.2 | <0.1 | 35.2 | 2.1 | 5.7 | 2.2 | |
| SX24 | 11.6 | 0.9 | 1.2 | 0.2 | <0.1 | 2.0 | 7.0 | <0.1 | 65.9 | 3.0 | 7.2 | 0.9 | |
| Q1k3 | 62.6 | 10.1 | 6.5 | <0.1 | 19.4 | <0.1 | <0.1 | <0.1 | <0.1 | <0.1 | <0.1 | <0.1 | unusual |
| Q1k4 | 25.8 | 10.6 | 7.7 | 1.9 | <0.1 | 22.5 | <0.1 | <0.1 | 29.2 | 1.8 | 0.2 | 0.1 | unusual |
| Q1k6 | 38.0 | 7.4 | 10.6 | 0.4 | <0.1 | 4.4 | 2.7 | <0.1 | 17.5 | 2.5 | 13.8 | 2.5 | |
| Q1k7 ROI1 | 40.6 | 5.1 | 4.8 | 1.2 | <0.1 | 13.0 | 11.9 | <0.1 | 16.9 | 2.1 | 1.9 | 2.2 | |
| Q1k7 ROI2 | 25.2 | 5.2 | 4.3 | 1.9 | <0.1 | 12.8 | 14.8 | <0.1 | 24.0 | 3.0 | 4.6 | 3.7 | |
| Q1k16 | 16.5 | 18.3 | 14.8 | 0.6 | <0.1 | 1.7 | 2.0 | <0.1 | 31.9 | 1.3 | 5.6 | 6.6 | |
| Q1k10 | 34.7 | 6.5 | 4.4 | 0.7 | <0.1 | 6.7 | 9.3 | <0.1 | 26.1 | 2.0 | 7.2 | 2.3 | |

Samples marked as unusual were not considered in the present study as they showed evidence of extensive hydrothermal alteration and are not representative of the 2nd member.
^aincludes proportion identified as mixed-layer illite/smectite.

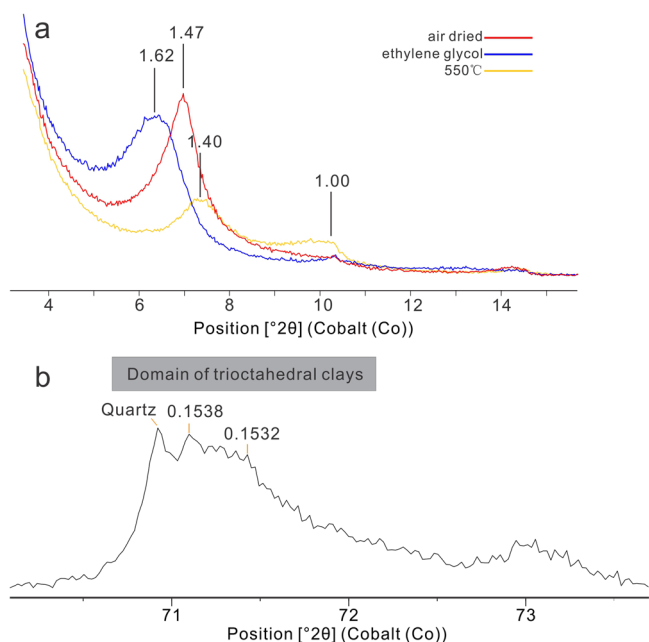


Fig. 3 Representative XRD patterns of the clay fraction (<2 μm). **a** Qlk7, position of the 001 peak of oriented, Ca-saturated air-dried sample. **b** SX22, powder XRD pattern of the <2 μm fraction showing the position of the 060 peak centered at ~1.53 nm, consistent with trioctahedral occupancy.

compaction deformation around silt-size quartz and dolomite grains (Fig. 4b, d, f). Individual saponite particles or flakes within laminae are oriented approximately parallel to bedding (Fig. 4b) whereas the saponite flakes in pore-fill domains appear more randomly oriented, consistent with variable compaction-induced orientation (Fig. 4d, g).

We distinguish two distinct chlorite types in our samples: (1) short, platy flakes <5 μm in length including some with fine-grained texture similar to saponite (Fig. 5a–c) and (2) larger flakes »5 μm in length with discrete boundary (Fig. 5d, e). Short-flake chlorite is present mainly in intergranular pore-fill domains (Fig. 5a, b), commonly in association with saponite and, more rarely, associated with partially altered feldspar (Fig. 5c) or intergrown with pyrite (Fig. 5b). Some individual short-flake chlorite particles are thicker than saponite flakes but, just like saponite, show varying degrees of orientation depending on silt bridging³² (Fig. 5a). In addition, short-flake chlorite domains are similar to saponite pore-fill domains, and saponite-chlorite intergrowths are common (Figs. 4d, f; 5a–c). Large chlorite flakes, by contrast, are discrete grains 7–60 μm in length that are oriented parallel to bedding, identical in shape and size to muscovite grains. Individual flakes commonly contain pyrite inclusions and, more rarely, show regions that are compositionally more similar to muscovite (Fig. 5d, e), suggesting chloritization of muscovite. Consistent with this, muscovite occurs usually in less altered samples (Fig. 5f). Overall, large-flake chlorite displays higher FeO and TiO₂ content compared to short-flake chlorite (Supplementary Fig. 2).

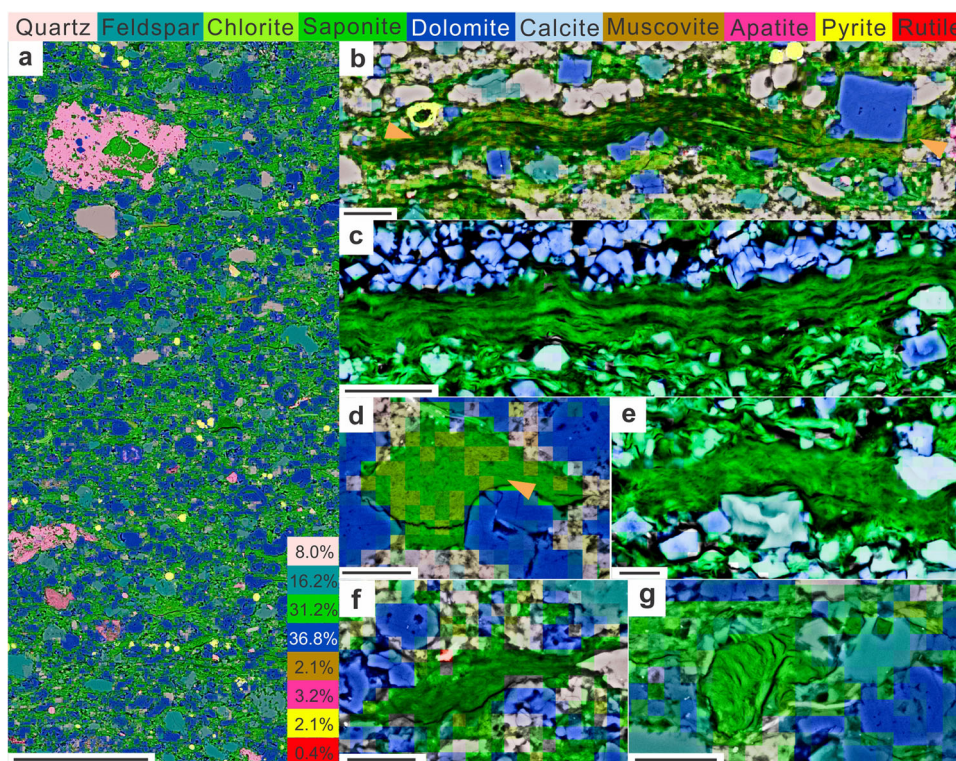


Fig. 4 SEM-EDS mineral mapping images of representative examples of saponite from the Doushantuo Formation and Green River Formation. Scale bars represent 100 μm in (a) and 10 μm for (b–g). **a** SX22, a 250*550 μm region providing overview of a saponite-rich and less altered sample. **b** Qlk7, wavy laminae of authigenic saponite particles (partially chloritized) displaying approximately bedding-parallel orientation of the fine clay crystals. Individual laminae are largely free of detrital grains and are curved due to burial compaction (yellow arrows). Saponite deformed around dolomite and other brittle grains by compaction (c) Laminae of bedding-parallel saponite in the Green River Formation, USA. **d** SX4, pore-filling saponite aggregate grain (partially chloritized) with randomly oriented individual clay particles. Some deformation from burial compaction (yellow arrow), but largely uncompacted due to silt bridging effect. **e** Randomly oriented saponite in the Green River Formation fills an intergranular pore. **f** SX17, intergranular pore-filling saponite with individual saponite particles partially oriented. **g** SX22, saponite intragranular pore-fill in feldspar.

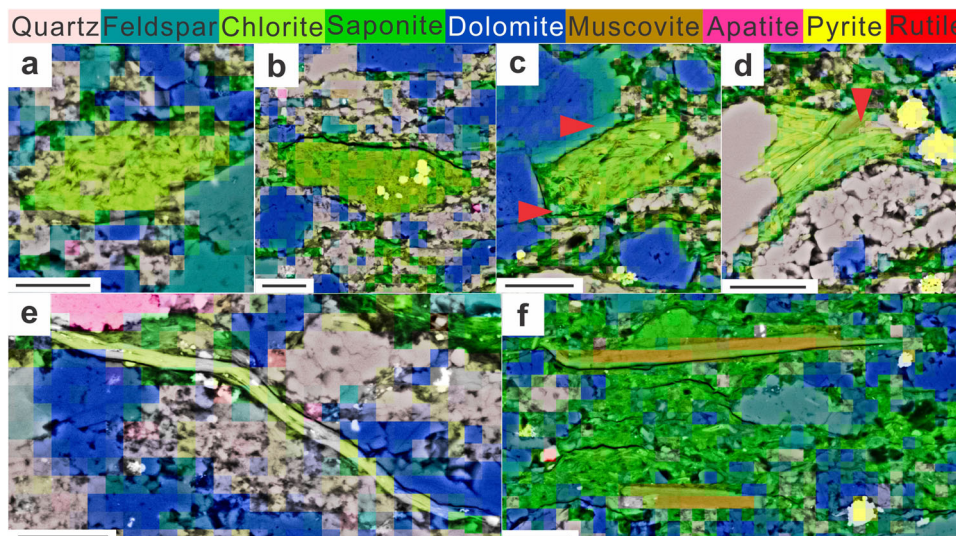


Fig. 5 SEM-EDS mineral mapping images of representative examples of chlorite and muscovite from the Doushantuo Formation. Scale bars represent 10 μm (a) SX12, randomly oriented, intergrown chlorite-saponite flakes filling a pore interpreted to be a fully chloritized saponite intergranular pore-fill similar to Fig. 4d, f. (b) Qlk10, partially oriented, chlorite-saponite pore-fill with similar texture as unaltered saponite and pyrite inclusions (c) Qlk7, chlorite with flaky texture replacing a feldspar grain. Note the feldspar residue at the top and the bottom left corner (red arrows) interpreted to be a fully chloritized saponite aggregate similar to Fig. 4g. (d) Qlk7, partially chloritized muscovite flakes (red arrow denotes muscovite residue). (e) SX4, long chlorite flake deformed by compaction. (f) SX22, long muscovite flakes parallel to bedding.

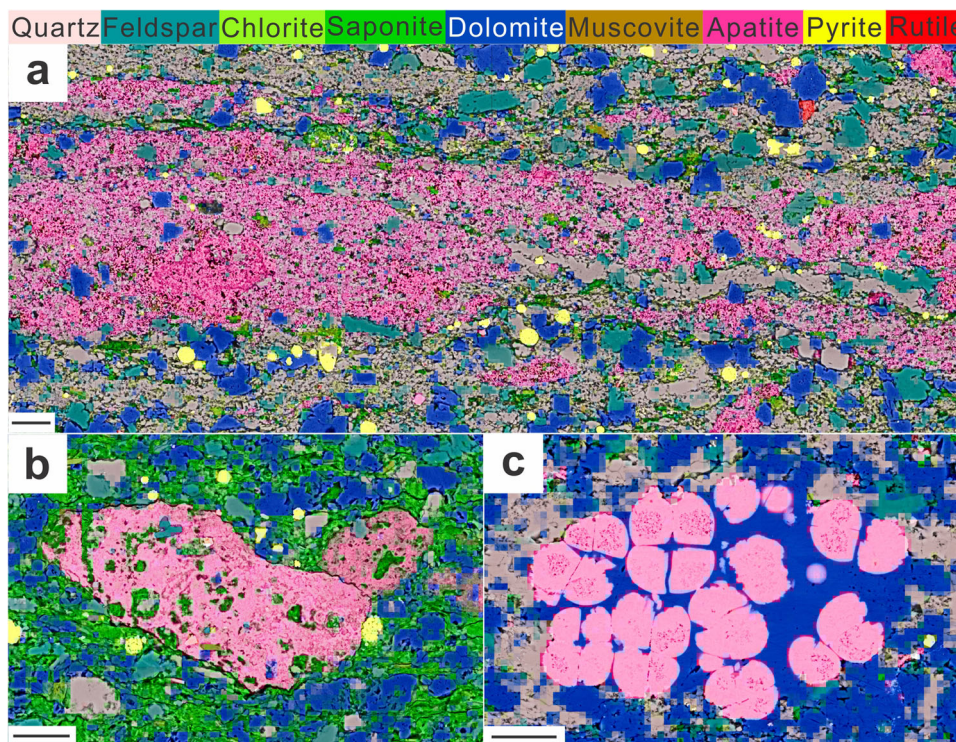


Fig. 6 SEM-EDS mineral mapping images of phosphatic laminae, nodules and fossils. Scale bars represent 20 μm . (a) SX22, phosphatic nodules with saponite, feldspar, quartz and dolomite inclusions. (b) SX4, phosphatic embryo-like fossils resembling *Archaeophycus yunnanensis*, preserved in a dolomite nodule. (c) Qlk6, phosphatic laminae associated with micro quartz and other mineral inclusions; framboidal and euhedral pyrite are both present.

Apart from clay minerals, silt-size clastic particles (quartz and feldspar), apatite and pyrite are also common in our samples. Quartz and feldspar account for 5.3–56.0 wt% of the mineral fraction in each sample, averaging 31.2 wt% (Table 1). In addition to clastic quartz, we also observe micro-crystalline quartz that is concentrated in laminae, often in association with apatite, saponite, or short-flake chlorite (Fig. 6a), as well as chert nodules ~5 mm in

size. Apatite content ranges from 0.2 to 13.8 wt% (average 3.6 wt%) and is concentrated in elongate, phosphatic nodules oriented parallel to bedding (Fig. 6b) or in laminae with micro-quartz (Fig. 6a). Both phosphatic nodules and laminae contain other minerals, including saponite, chlorite, quartz, feldspar and dolomite. In addition, phosphatic fossils (Fig. 6c) were observed in several samples (SX4, SX12 and Qlk6), where they most commonly occur

as dolomite or authigenic feldspar cemented clusters. These first occur ~22 m above the lower boundary of the 2nd member, and are identified as *Archaeophycus yunnanensis*³³. Framboidal pyrite is common in all samples, with minor euhedral pyrite and micro-pyrite inclusions in chlorite or muscovite flakes also occurring (Fig. 6a, b). The total pyrite content ranges from 0.8 to 6.6 wt%, averaging 2.5 wt%.

Origins of clay minerals. Our petrographic evidence identifies a pre-compaction origin for saponite in the Doushantuo Formation (Supplementary Table 1). Firstly, saponite in most samples is concentrated in domains exceeding 10 μm in size (Fig. 4a). Primary (i.e. intergranular) pores of this size rarely survive compaction and burial in mudstones³⁴, so that the saponite fill must predate burial-induced compaction. Consistent with this, compaction has impacted on both saponite laminae and intergranular pore-fill domains. Individual saponite particles in laminae exhibit bedding parallel orientation, consistent with compaction, whereas pore-fill domains are partially sheltered so that individual particles are randomly orientated except where pore-fill is deformed around resistant grains³². Clays of hydrothermal origin, by contrast, post-date compaction and are therefore expected to be randomly or radially oriented regardless of domain type (laminae vs intergranular pore) or proximity to resistant grains. We therefore conclude that the above properties demonstrate a pre-compaction origin for saponite, ruling out burial diagenesis or hydrothermal alteration origins.

Both detrital and authigenic clays are of pre-compaction origin, but can be distinguished petrographically (Supplementary Table 1). Detrital saponite is sourced from pedogenic weathering of (ultra)mafic silicates¹⁸ and undergoes erosion and transportation together with other weathering products prior to deposition. Detrital saponite would therefore be expected to settle together with other detrital weathering products. However, not only is saponite concentrated in domains that are largely devoid of any detrital material, the fragile nature of the individual elongate, sheet-like saponite particles means that these are unlikely to survive transport without modification, further arguing against a detrital origin. In addition, since the sheet-like structure of clay particles typically results in preferential orientation after settling through the water column³⁵, the random orientation of individual pore-fill saponite particles also argues against a detrital origin. Saponite is commonly associated with and deformed around silt-size dolomite (dolomicrite; Fig. 4a). Previous work has shown that dolomicrite in the 2nd member of the Doushantuo Formation is of syndepositional, earliest diagenetic origin³⁶. Deformation of saponite around dolomite grains could therefore be partially due to early fabric displacing dolomite growth, but is likely mainly due to burial compaction. Together, the above observations strongly argue for an authigenic origin for the Doushantuo saponite. This conclusion is further supported by the striking similarity between the saponite morphology and distribution in the Doushantuo Formation and the demonstrably authigenic saponite domains observed in representative samples of the Green River Formation (Fig. 4c, e;²²).

We infer that the authigenic saponite laminae formed at the sediment-water interface or, alternatively, as early diagenetic replacements of detrital clay or gel precursors¹⁹, whereas the intergranular pore-filling authigenic saponite precipitated from pore water shortly after sediment deposition. The intragranular saponite in feldspar is authigenic pore-fill associated with early diagenetic feldspar dissolution. A late stage hydrothermal alteration origin¹² for this feldspar-associated saponite can be ruled out because a) the samples with the greatest abundance of feldspar-associated saponite do not show any evidence for

hydrothermal alteration (i.e. extensive chloritization) and b) EPMA results (Supplementary Fig. 2, Supplementary Data 2) reveal that these are compositionally indistinguishable from laminae or intergranular-pore hosted authigenic saponite. In conclusion, the Doushantuo saponite was formed syn-depositionally or during earliest diagenesis, with the required chemical constituents sourced from bottom water and from early diagenetic dissolution of detrital silicates (see extended discussion in next section).

What then is the significance of the saponite-chlorite intergrowths? Short-flake chlorite is compositionally and texturally similar to authigenic saponite (Figs. 4d, f, g; 5a–c). In addition, mineral mapping shows that saponite-chlorite intergrowths are widespread (Fig. 4b, d) and XRD analysis identifies the ubiquitous presence of mixed-layer chlorite-smectite (Fig. 3a). Previous work documents a regional hydrothermal event centered on the underlying Nantuo Formation and cap dolostones³⁷, and this has been shown to have caused alteration in the 2nd member of the Doushantuo Formation, showing increased chloritization downward toward the cap carbonate³⁸. Consistent with this, we interpret short-flake chlorite and chlorite-saponite mixed layer as hydrothermal alteration products of authigenic saponite^{38,39}, and infer that chlorite-enriched samples are relatively more hydrothermally altered than samples with lower proportions of chlorite. Long-flake chlorite, by contrast, is most likely a pseudomorphic alteration product of muscovite²⁸, as supported by their particle morphology and the occasional presence of residual muscovite (Fig. 5d). The sample with largest proportion of muscovite (SX22, Table 1) contains no chlorite further supporting an alteration origin for long-flake chlorite. Strikingly this sample (SX22) contains only ~2 wt% muscovite, underscoring the scarcity of detrital phyllosilicates in the 2nd member of the Doushantuo Formation.

In summary, we are able to distinguish the origins of Doushantuo clays based on their distinct petrographic and geochemical characteristics. We demonstrate that clay minerals of both detrital (muscovite) and authigenic (saponite) origins were present prior to compaction, and both were affected by partial post-compaction alteration to chlorite or chlorite-saponite mixed layer (Supplementary Fig. 3). The authigenic saponite formed syn-depositionally or during earliest diagenesis, in response to favourable basinal bottom water or pore water conditions and represents the dominant phyllosilicate constituent in the 2nd member.

Implications for Paleo-Environmental Setting and Reverse Weathering. Two fundamentally different paleo-environmental settings have been proposed to explain the spatially restricted abundance of saponite in the 2nd member of the Doushantuo Formation: (1) a proximal marine setting which received an abundance of weathered (ultra)mafic detritus including pedogenic saponite⁸ or (2) an alkaline (pH > 9) lake setting which favored the precipitation of authigenic saponite⁷. Our results, when considered together with published constraints, argue against both of these scenarios.

Firstly, while the detrital fraction of the 2nd member may well have a mixed igneous to (ultra)mafic provenance, detrital saponite is essentially absent, with the detrital constituents consisting mainly of quartz and feldspar rather than phyllosilicates. Meanwhile, authigenic saponite makes up ~70 wt% of the clay content throughout the 2nd member in the YGA. Since the vast majority of Phanerozoic sedimentary saponite deposits are associated with evaporitic, alkaline lake settings^{40,41} this might seem to support a similar lacustrine setting for the saponite in the YGA. However, published carbonate-hosted Sr isotope values

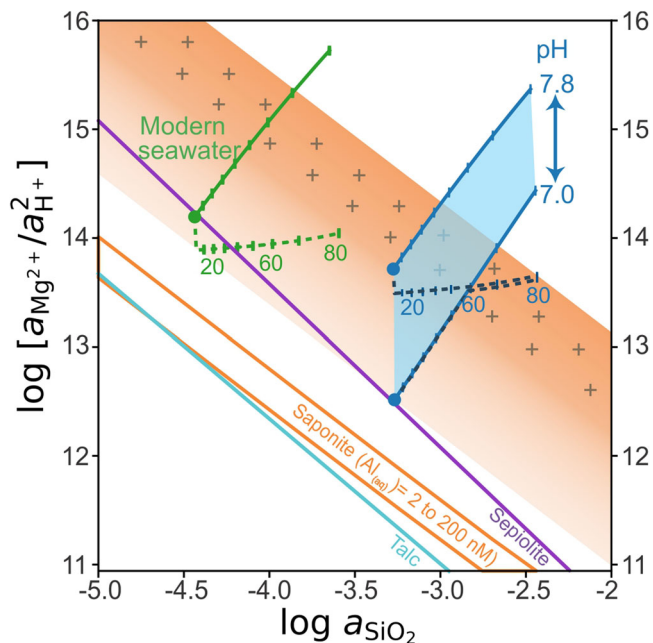


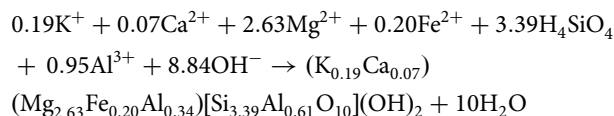
Fig. 7 Stability diagram of saponite and modeled evaporation pathways.

Modern seawater (green) and Ediacaran seawater (blue). Talc stability boundary (turquoise), saponite stability boundary (orange), and sepiolite stability boundary (purple) are shown as a function of dissolved Mg, H, and Si activities. Filled circles represent starting conditions (0 evaporation), solid lines represent evaporation pathway with no mineral precipitation, and dashed lines represent evaporation pathways considering calcite precipitation (each hash along the two lines represents a 10% step in evaporation). Two different pH starting conditions are modeled for Ediacaran seawater (7.0 and 7.8) to create the envelope of potential results. Orange gradient shading is parallel to saponite stability lines and its upper and lower boundary cross the starting point at 7.0 pH and 80% evaporation point with calcite precipitation of Ediacaran seawater pathway, respectively. The area with plus sign pattern shows the differences between modern and Ediacaran seawater after 80% evaporation, and represents potential range of the critical supersaturation. Temperature = 25 °C, $p\text{CO}_2 = 10^{-3}$ bar.

(0.7078–0.7082, radiogenic values outside this range are restricted to a narrow interval in the uppermost 2nd member)⁴² are centered around the expected lower Ediacaran seawater value of ~0.708⁴³ and REEs measured in chert also demonstrate a seawater-like pattern for the 2nd member⁴⁴. These observations argue against an alkaline lake setting. Moreover, the abundant presence of pyrite (up to 6.6 wt%, average 2.5 wt%) as well as the ubiquitous co-occurrence and common intergrowth of authigenic saponite, pyrite and apatite (Fig. 6a, b) also argue against such a lacustrine setting. Abundant pyrite formation usually implies a marine sulfate source and, since the solubility of apatite increases greatly with the incorporation of carbonate anions⁴⁵, the predominance of the carbonate ion under highly alkaline conditions is expected to inhibit carbonate fluorapatite formation⁸. Individually, any of these observations may sporadically occur in specific lake settings (e.g. pyrite in volcanically fed lakes⁴⁶, minor apatite deposition during early diagenesis in alkaline lakes⁴⁷), however the persistently marine character of each of these lines of evidence throughout the 2nd member collectively argues against a lake setting, even a lake with intermittent marine connection⁷.

Given that an isolated lake setting is incompatible with the available geochemical and mineralogical evidence, could Ediacaran seawater composition have permitted the formation of saponite in the YGA? To guide our discussion, we consider the

ingredients required for saponite formation via a reverse weathering reaction, with YGA saponite composition constrained by our EPMA data (Supplementary Data 2):



Ediacaran seawater can likely provide sufficient H_4SiO_4 , Mg^{2+} , K^+ and Ca^{2+} , but the low aqueous concentrations of Al^{3+} and Fe^{2+} under typical marine conditions suggest that these would have had to come from the dissolution of clastic detritus⁴⁸. Reductive dissolution of ferric oxyhydroxides coupled to microbial organic carbon remineralisation is a likely source of Fe^{2+} in the pore fluid⁴⁹, consistent also with the presence of abundant pyrite. The ubiquitous early diagenetic saponite infilling of feldspar pores supports the idea that dissolution of feldspar and, potentially, detrital clays provided the Al^{3+} ions required to form saponite (Fig. 4g).

Thermodynamic considerations indicate that the activity of the dissolved H_4SiO_4 and Mg^{2+} species as well as fluid pH are key for forming authigenic Mg-silicates⁴⁸, including saponite. In the absence of a large biological sink for silica, early Ediacaran seawater was likely characterized by elevated H_4SiO_4 compared to the present⁵⁰ and therefore would have been more favorable to clay authigenesis (i.e., reverse weathering²⁴). Elevated seawater H_4SiO_4 is supported by the widespread occurrence of silica cements (Fig. 6a) and chert nodules in the Doushantuo Formation⁵¹. Similarly, Neoproterozoic seawater was likely characterized by greater Mg^{2+} concentrations compared to Cambrian seawater, with marine carbonate cement evidence for high Mg/Ca conditions and widespread, potentially primary, dolomite⁵². Consistent with this, thermodynamic calculations indicate that saponite was most likely supersaturated in Ediacaran seawater (Fig. 7). However, the scarcity of sedimentary saponite in Neoproterozoic marine sequences (we are aware of only one report outside of the YGA⁵³), and the absence of saponite in time-equivalent lower Doushantuo sediments deposited in unambiguously marine slope to basin settings⁷ shows that the abundance of authigenic saponite we document in the YGA cannot simply be a product of favorable Precambrian seawater composition. We therefore conclude that the spatially restricted, regional abundance of saponite argues against a typical open marine setting for the YGA. This interpretation is further supported by geochemical evidence documenting major differences between the YGA and coeval slope to basin (open marine) settings, including the relatively low abundance of water-column sourced redox-sensitive trace elements⁷ as well as the distinct stratigraphic trends of $\delta^{15}\text{N}$, $\delta^{34}\text{S}$ and $\delta^{13}\text{C}_{\text{carb}}$ in the YGA^{27,54,55}.

Given the above, how do we explain the abundance of saponite in the YGA? We attribute the restricted distribution of saponite to kinetic inhibition of Mg-silicate precipitation⁵³, possibly because Ediacaran seawater pH was lower (less alkaline) than is favorable for saponite precipitation^{56,57}. The precipitation of saponite from lower pH but highly Si and Mg enriched fluids (e.g. low-temperature off-axis hydrothermal settings¹⁵) suggests that a further increase in $a[\text{H}_4\text{SiO}_4]$ and $a[\text{Mg}^{2+}]$, for example via evaporative concentration beyond a ‘critical supersaturation’, can help to overcome a kinetic barrier^{58,59} (Fig. 7). That is, conditions only slightly exceeding the saponite stability curve may not be enough to overcome additional constraints (e.g. kinetic controls). The real-world precipitation of saponite likely requires a greater degree of supersaturation (larger distance from saponite stability curve) as would be the case for Ediacaran seawater because of its higher silica content than modern seawater (Fig. 7). To test this,

we used reaction path modeling, constrained by existing estimates of Ediacaran seawater composition (0.5–1.0 mM silica^{50,60} and pH of 7.0–7.8⁵⁷), which offers support for our hypothesis. This modeling demonstrates that seawater becomes increasingly supersaturated with respect to Mg-silicates including saponite, talc and sepiolite with progressive evaporative concentration (solid blue lines in Fig. 7), even if we allow for pH buffering through calcite precipitation (dashed blue lines in Fig. 7). We attribute the absence of talc in the YGA samples to elevated pore water Al (sourced from the dissolution of Al-rich debris such as feldspar and clays), which would inhibit precipitation of non-aluminous talc and other hydrous Mg-silicates, favoring saponite formation^{48,59}. Moreover, modelled pH remains below 8.5 (Supplementary Fig. 4), a critical kinetic threshold for talc precipitation⁵³, further inhibiting talc formation. In the presence of a dissolved Al pool, both the tetrahedral and octahedral sheets of a newly forming clay mineral incorporate structural Al, producing charge imbalances in these layers. These imbalances drive the formation of an interlayer sheet, meaning that smectite-type clays preferentially form¹¹. Such smectites preferentially sorb K^+ from the pore water⁵⁸, which expresses in the formation of K-intercalated clays. This is consistent with K-saponite in our samples (Supplementary Fig. 2). Early diagenetic microbial sulfate reduction and organic matter decay ($SO_4^{2-} + 2CH_2O \rightarrow H_2S + 2CO_2 + 2OH^-$) would have also contributed to saponite formation, further increasing pore water pH, whereas sulfide production favored pyrite formation before exhaustion of marine sulfate⁵¹ allowed accumulation of dissolved Fe^{2+} ¹⁰. The dominance of bivalent (Mg^{2+} , Fe^{2+}) over trivalent (Al^{3+} , Fe^{3+}) ions in the pore water resulted in the formation of a trioctahedral clay, and is consistent with the K-saponite containing some Fe^{2+} which occasionally intergrow with pyrite (Fig. 5b). Dioctahedral clays arguably did not form because of $Mg^{2+}/Fe^{2+} \gg Al^{3+}$, preventing the formation of montmorillonite⁴⁸, and $Fe^{2+} \gg Fe^{3+}$, preventing the formation of nontronite¹⁷.

Existing paleo-geographic models suggest that an expansive, carbonate-rimmed intrashelf basin or lagoon covered a substantial portion of the Yangtze Block⁹. We hypothesize that a restricted, modestly evaporitic (degree of evaporation <90% because of absence of evaporite phases such as gypsum in the Doushantuo Formation⁶¹) but marine-influenced shelf lagoon setting would have provided the highly supersaturated conditions required for the precipitation of saponite (Fig. 7). This is supported by paleo-magnetic data which place South China at ~30°N from 635 Ma to 560 Ma⁶², a mid-latitude position (high evaporation, low rainfall) which would have contributed to the evaporative concentration of already Si- and Mg-rich Ediacaran seawater^{50,63}, as well as a modest increase in pH⁶⁴.

What are the implications of our findings in the context of recent work arguing that reverse weathering was much expanded in the Precambrian oceans? As noted above, the apparent absence of saponite in slope to basinal equivalents of the 2nd member of the Doushantuo demonstrates that Ediacaran seawater was insufficiently enriched in key ingredients to form saponite in open marine settings. However, reaction path modelling suggests that the striking, ~40 Myr dominance of authigenic saponite in the lower Doushantuo of the YGA required not only specific local environmental conditions facilitating evaporative concentration of seawater, but relied also on seawater composition favoring marine-influenced authigenic clay formation. We suggest that the enriched nature of Precambrian seawater allowed saponite to reach critically supersaturated conditions with only modest evaporation. However, the critical threshold for saponite precipitation cannot be reached by evaporation of Si-depleted Phanerozoic seawater, consistent with the absence of saponite in Phanerozoic marine evaporites. This is supported by reaction

path modelling which shows that Ediacaran seawater is more saturated with respect to saponite than modern seawater for all but the lowest estimates for Ediacaran seawater pH (Fig. 7). We stress that this is a conservative estimate, as our model assumes a conservative Ediacaran seawater composition (0.5 mM H_4SiO_4 , modern-like Mg). Our results therefore provide indirect support for the Precambrian reverse weathering hypothesis²⁴, implying that authigenesis of low-Mg but Fe- and K-rich marine clays occurred more widely outside of evaporitic settings, with implications for the global carbon cycle, marine elemental cycles and planetary climate^{24,29,65,66}. While systematic additional work is required to address the full extent of these implications, our study demonstrates the tools and an approach with which to robustly test for the predicted widespread abundance of authigenic clays.

Impact of restricted lagoon environment on Doushantuo Biota

How might a restricted and evaporitic lagoonal setting have influenced the Doushantuo biota? The 2nd member of the Doushantuo Formation hosts various phosphatically or siliceously preserved multicellular acritarchs^{3,67}, including embryo-like fossils which are potential candidates for the earliest animal life on Earth⁴. Strikingly, fossil-bearing localities in the lower Doushantuo are largely restricted to shelf lagoon and shelf margin settings, and rare in the deeper slope to basin⁹ (Fig. 1). This pattern has been attributed to challenging conditions including widespread anoxia in the Neoproterozoic Ocean^{7,68}, but our results indicate an additional role for water chemistry. The lagoon setting is likely to have provided an unusually favorable environment for prokaryotic and eukaryotic organisms (including, potentially, metazoans) as it would have facilitated accumulation of nutrients such as phosphorous that were in scarce supply in the early Ediacaran Ocean⁶⁹. Geochemical proxy-based evidence indicates that the Yangtze Lagoon received riverine inputs from weathering of a mafic to ultra-mafic hinterland⁸, lithologies associated with elevated P- and trace metal contents⁷⁰. Limited exchange between the lagoon and the open ocean would have contributed to the retention and build-up of these terrestrial-runoff derived nutrients⁷¹. A local build-up of P and other nutrients derived from terrestrial runoff is also supported by paleo-geographic reconstructions showing that phosphatic intervals in the Doushantuo Formation are almost entirely restricted to shallow-water lagoonal environments^{9,72}. These intervals are rare in the deeper slope and basin localities, regions which would have received abundant P if nutrient distribution was being dominantly controlled by upwelling⁹. An abundance of terrestrially derived P and evaporatively concentrated marine Si would also have contributed to the preservation of the Doushantuo fossils^{7,73}. Finally, the evolution of these organisms in a restricted basin and subsequent adaptation to the lagoon's unique water chemistry may also explain the high degree of endemism of the lower Doushantuo biota^{9,72}, similar to the ecological impact of an alkaline lake setting proposed by Bristow et al.⁷. Their subsequent radiation and expansion into open marine environments would have been facilitated by the gradual rise in marine nutrients (including P,⁶⁹) as well as dissolved oxygen over the Ediacaran, which ultimately set the scene for the major environmental and biological changes that ushered in the Phanerozoic⁷⁴.

Conclusion

In summary, the distinct petrographic and geochemical features we present here confirm the ubiquitous presence of abundant, syn-depositional authigenic saponite in the 2nd member of Doushantuo Formation. The spatially restricted distribution of saponite and marine geochemical signatures in the YGA

combined with paleo-geographic reconstructions imply a shelf lagoon setting at mid latitude. Modest evaporation within the lagoon would have concentrated key seawater constituents (Mg^{2+} , H_4SiO_4 and OH^-) in the lagoon beyond a critical supersaturation threshold, facilitating the formation of saponite. This lagoonal setting could have also allowed for the accumulation of key nutrients such as phosphorous from terrestrial runoff, providing a favourable environment for earliest metazoan life. Furthermore, the occurrence of authigenic saponite also supports the hypothesis that silica-rich Precambrian seawater was favourable for reverse weathering.

Materials and methods

Samples. Nineteen samples were selected from the shale interbeds of the 2nd member at two different sites in the YGA (Fig. 2), namely, the Sixi Section (30°45'25.8" N, 110°55'51.0" E) and the Qinglinkou Section (30°48'0.2" N, 110°55'18.5" E). No sampling permissions were required. In addition, several samples of a classic alkaline, evaporitic lake sequence rich in authigenic saponite (Parachute Creek Member of the Eocene Green River Formation, USA) were studied for comparison (see ref. 22 for sample details). All samples were cut into blocks with a 1–2 cm² surface perpendicular to the bedding plane and prepared as polished mounts for subsequent scanning electron microscope imaging and mineral mapping.

Samples for powder X-ray diffraction (XRD) were crushed in a Rock Labs RM100 Disc Mill and micronized using a McCrone mill, with the addition of ethanol. Four samples with relatively high clay content based on the bulk XRD results were selected for further identification of the clay mineral suite. For the clay mineral separation, 5 g of crushed sample was reacted overnight with 1 M acetic acid-sodium acetate buffer in a 70 °C water bath to remove the carbonate fraction before centrifugal separation of the clay size (<2 µm) fraction and Ca saturation³⁰.

X-Ray Diffraction. Powder X-ray diffraction patterns spanning 3.5° to 95° 2θ were collected using a Malvern Panalytical Aeris tabletop XRD instrument (Co radiation source with 40 kV generator voltage and 15 mA current, PIXcel3D-Medipix3 1×1 detector) with 0.022° step size. Oriented, air dried clay films were analysed from 2° to 40° 2θ with the same equipment, followed by analysis after treatment with ethylene glycol and heating to 550 °C. Rietveld-based quantification of PXRD patterns was conducted via the Panalytical Highscore Plus Software and its implemented pdf-4 database with an uncertainty of <3%.

Scanning electron microscope and mineral mapping. Backscatter electron (BSE) images and mineral maps were obtained with a FEI Teneo LoVac field emission scanning electron microscope (SEM) equipped with dual Bruker XFlash Series 6 energy dispersive X-ray spectroscopy (EDS) detectors. BSE images of the entire sample (100 nm pixel resolution) and EDS spectra (2 µm step size, 8 ms acquisition time) for mineral mapping of smaller regions of interest were obtained using the FEI Maps Mineralogy software, followed by classification of the individual EDS spectra using the FEI Nanomin software (FEI Nanomin/Maps Mineralogy^{28,29}). Unlike other SEM-based mineral mapping techniques (e.g. QEMSCAN), the Nanomin mineral classification system can deconvolve mixed X-ray spectra and assign up to three minerals per analysed spot. This is a critical requirement for the correct interpretation of the mixed phase X-ray spectra characteristic of heterogeneous fine-grained sediments, where the X-ray generating electron interaction volume is commonly larger than the grain size. Mineral concentrations (reported as wt%) in the mapped areas are determined by converting the mineral area% to wt% using published densities for all identified sample constituents, with accuracy and precision comparable to quantitative XRD analysis²⁸. Comparison of quantitative mineralogy from SEM-EDS mineral mapping to constraints from quantitative XRD shows near-identical results, demonstrating the accuracy of SEM-EDS mineral identification (Supplementary Fig. 1, Supplementary Data 1).

Electron probe micro analysis. Electron probe micro analysis was applied on two representative samples (SX2 and Qk7) to validate the petrographic classification of clay types, using a Cameca SX-100 electron microprobe at 15kV, 20 nA and spots sizes of 2–5 µm (See supplementary Data 2 for the standard information).

Hydrochemical modelling. To better constrain the potential depositional setting, hydrochemical modelling was applied to test the thermodynamic feasibility of forming Mg-silicates (including saponite) from seawater-derived fluids and contribution of modest evaporation (0–80%, Fig. 7), both with and without carbonate precipitation. We also compare the evaporation pathway of modern seawater with inferred Ediacaran seawater. While Ediacaran seawater remains poorly constrained, studies have suggested that seawater at this time had a pH ~7.8, and possibly as low as 7.0⁵⁷, with silica content between 0.5 and 1.0 mM^{50,60}. For this model, we ran Ediacaran seawater with a starting pH value of 7.0 and 7.8, and assume a conservative silica content of 0.5 mM and a magnesium content of 52 mM⁶³. Our

starting values for modern seawater are pH = 8.04, silica content of 0.035 mM⁵³ and Mg^{2+} content of 55 mM⁷⁵.

The chemical evolution of seawater with evaporation as well as relevant stability boundaries were calculated assuming thermodynamic equilibrium. Modeling was carried out in PHREEQC v3.7.1⁷⁶. Mineral stabilities were evaluated using the carfbx.dat database⁷⁷. The saponite stability boundary was evaluated for the Mg, K, and Na endmembers of Mg-saponite⁷⁸. The pitzer.dat database with its Pitzer specific-ion-interaction aqueous model was used for seawater evaporation pathways due to its suitability for high salinity fluids. The pathways assume temperature of 25 °C, $p\text{CO}_2$ of 10⁻³ bar and thermodynamic equilibrium with calcite at all times.

Data availability

All relevant data of this study are included in the article and/or <https://doi.org/10.6084/m9.figshare.19919321>⁷⁹.

Received: 3 November 2021; Accepted: 7 July 2022;

Published online: 25 July 2022

References

- Condon, D. U-Pb ages from the Neoproterozoic Doushantuo Formation, China. *Science* **308**, 95–98 (2005).
- Xiao, S., Zhang, Y. & Knoll, A. H. Three-dimensional preservation of algae and animal embryos in a Neoproterozoic phosphorite. *Nature* **391**, 553–558 (1998).
- Chuanming, Z., Guwei, X., McFadden, K., Shuhai, X. & Xunlai, Y. The diversification and extinction of Doushantuo-Pertatataka acritarchs in South China: causes and biostratigraphic significance. *Geol. J.* **42**, 229–262 (2007).
- Yin, Z., Zhu, M., Bottjer, D. J., Zhao, F. & Tafforeau, P. Meroblastic cleavage identifies some Ediacaran Doushantuo (China) embryo-like fossils as metazoans. *Geology* **44**, 735–738 (2016).
- Cunningham, J. A., Vargas, K., Yin, Z., Bengtson, S. & Donoghue, P. C. J. The Weng'an Biota (Doushantuo Formation): an Ediacaran window on soft-bodied and multicellular microorganisms. *J. Geol. Soc.* **174**, 793–802 (2017).
- Bowyer, F., Wood, R. A. & Poulton, S. W. Controls on the evolution of Ediacaran metazoan ecosystems: A redox perspective. *Geobiology* **15**, 516–551 (2017).
- Bristow, T. F. et al. Mineralogical constraints on the paleoenvironments of the Ediacaran Doushantuo Formation. *Proc. Natl. Acad. Sci.* **106**, 13190–13195 (2009).
- Huang, J., Chu, X., Lyons, T. W., Planavsky, N. J. & Wen, H. A new look at saponite formation and its implications for early animal records in the Ediacaran of South China. *Geobiology* **11**, 3–14 (2013).
- Jiang, G., Shi, X., Zhang, S., Wang, Y. & Xiao, S. Stratigraphy and paleogeography of the Ediacaran Doushantuo Formation (ca. 635–551 Ma) in South China. *Gondwana Res.* **19**, 831–849 (2011).
- McFadden, K. A. et al. Pulsed oxidation and biological evolution in the Ediacaran Doushantuo Formation. *Proc. Natl. Acad. Sci.* **105**, 3197–3202 (2008).
- Chamley, H. *Clay Sedimentology*. (Springer Berlin Heidelberg, 1989). <https://doi.org/10.1007/978-3-642-85916-8>.
- Dill, H. G., Dohrmann, R. & Kaufhold, S. Disseminated and faultbound autohydrothermal ferroan saponite in Late Paleozoic andesites of the Saar-Nahe Basin, SW Germany: Implications for the economic geology of intermediate (sub)volcanic rocks. *Appl. Clay Sci.* **51**, 226–240 (2011).
- Nimis, P., Tesalina, S. G., Omenetto, P., Tartarotti, P. & Lerouge, C. Phyllosilicate minerals in the hydrothermal mafic/ultramafic-hosted massive-sulfide deposit of Ivanovka (southern Urals): comparison with modern ocean seafloor analogues. *Contrib. Mineral. Petrol.* **147**, 363–383 (2004).
- Post, J. L. Saponite from Near Ballarat, California. *Clays Clay Miner.* **32**, 147–153 (1984).
- Voigt, M., Pearce, C. R., Fries, D. M., Baldermann, A. & Oelkers, E. H. Magnesium isotope fractionation during hydrothermal seawater-basalt interaction. *Geochim. Cosmochim. Acta* **272**, 21–35 (2020).
- Grauby, O., Petit, S., Decarreau, A. & Baronnet, A. The nontronite-saponite series: an experimental approach. *Eur. J. Mineral.* **6**, 99–112 (1994).
- Cuadros, J. et al. Crystal-chemistry of interstratified Mg/Fe-clay minerals from seafloor hydrothermal sites. *Chem. Geol.* **360–361**, 142–158 (2013).
- Lessovaia, S. N. & Polekhovskiy, Yu. S. Mineralogical composition of shallow soils on basic and ultrabasic rocks of East Fennoscandia and of the Ural Mountains, Russia. *Clays Clay Miner.* **57**, 476–485 (2009).
- Milesi, V. P. et al. Formation of magnesium-smectite during lacustrine carbonates early diagenesis: Study case of the volcanic crater lake Dziani Dzaha (Mayotte - Indian Ocean). *Sedimentology* **66**, 983–1001 (2019).

20. Akbulut, A. & Kadir, S. The geology and origin of sepiolite, palygorskite and saponite in Neogene lacustrine sediments of the Serinhisar-Acipayam Basin, Denizli, SW Turkey. *Clays Clay Miner.* **51**, 279–292 (2003).
21. Furquim, S. A. C., Graham, R. C., Barbiero, L., de Queiroz Neto, J. P. & Vallès, V. Mineralogy and genesis of smectites in an alkaline-saline environment of Pantanal wetland, Brazil. *Clays Clay Miner.* **56**, 579–595 (2008).
22. Bristow, T. F., Kennedy, M. J., Morrison, K. D. & Mrofká, D. D. The influence of authigenic clay formation on the mineralogy and stable isotopic record of lacustrine carbonates. *Geochim. Cosmochim. Acta* **90**, 64–82 (2012).
23. Deocampo, D. M., Cuadros, J., Wing-dudek, T., Olives, J. & Amouric, M. Saline lake diagenesis as revealed by coupled mineralogy and geochemistry of multiple ultrafine clay phases: Pliocene Olduvai Gorge, Tanzania. *Am. J. Sci.* **309**, 834–868 (2009).
24. Isson, T. T. & Planavsky, N. J. Reverse weathering as a long-term stabilizer of marine pH and planetary climate. *Nature* **560**, 471–475 (2018).
25. Jiang, G., Kaufman, A. J., Christie-Blick, N., Zhang, S. & Wu, H. Carbon isotope variability across the Ediacaran Yangtze platform in South China: Implications for a large surface-to-deep ocean $\delta^{13}\text{C}$ gradient. *Earth Planet. Sci. Lett.* **261**, 303–320 (2007).
26. Lu, M. et al. The DOUNCE event at the top of the Ediacaran Doushantuo Formation, South China: broad stratigraphic occurrence and non-diagenetic origin. *Precambrian Res.* **225**, 86–109 (2013).
27. Wang, X., Jiang, G., Shi, X., Peng, Y. & Morales, D. C. Nitrogen isotope constraints on the early Ediacaran ocean redox structure. *Geochim. Cosmochim. Acta* **240**, 220–235 (2018).
28. Rafiei, M., Löhr, S., Baldermann, A., Webster, R. & Kong, C. Quantitative petrographic differentiation of detrital vs diagenetic clay minerals in marine sedimentary sequences: implications for the rise of biotic soils. *Precambrian Res.* **350**, 105948 (2020).
29. Abbott, A. N., Löhr, S. & Trethewey, M. Are Clay minerals the primary control on the oceanic rare earth element budget? *Front. Mar. Sci.* **6**, 504 (2019).
30. Moore, D. M. & Reynolds, R. C., Jr. *X-ray diffraction and the identification and analysis of clay minerals*. (Oxford University Press (OUP), 1989).
31. Baldermann, A. et al. The Fe-Mg-saponite solid solution series – a hydrothermal synthesis study. *Clay Miner.* **49**, 391–415 (2014).
32. Schneider, J., Flemings, P. B., Day-Stirrat, R. J. & Germaine, J. T. Insights into pore-scale controls on mudstone permeability through resedimentation experiments. *Geology* **39**, 1011–1014 (2011).
33. Xiao, S. et al. The Weng’an biota and the Ediacaran radiation of multicellular eukaryotes. *Natl. Sci. Rev.* **1**, 498–520 (2014).
34. Chalmers, G. R. L. & Bustin, R. M. Porosity and pore size distribution of deeply-buried fine-grained rocks: Influence of diagenetic and metamorphic processes on shale reservoir quality and exploration. *J. Unconv. Oil Gas Resour.* **12**, 134–142 (2015).
35. Meade, R. H. *Removal of water and rearrangement of particles during the compaction of clayey sediments - Review*. 497-B <https://pubs.er.usgs.gov/publication/pp497B> (1964).
36. Chang, B. et al. Massive formation of early diagenetic dolomite in the Ediacaran ocean: Constraints on the “dolomite problem”. *Proc. Natl. Acad. Sci.* **117**, 14005–14014 (2020).
37. Bristow, T. F., Bonifacie, M., Derkowski, A., Eiler, J. M. & Grotzinger, J. P. A hydrothermal origin for isotopically anomalous cap dolostone cements from south China. *Nature* **474**, 68–71 (2011).
38. Derkowski, A. et al. Hydrothermal alteration of the Ediacaran Doushantuo Formation in the Yangtze Gorges area (South China). *Geochim. Cosmochim. Acta* **107**, 279–298 (2013).
39. Beaufort, D. et al. Chlorite and chloritization processes through mixed-layer mineral series in low-temperature geological systems – a review. *Clay Miner.* **50**, 497–523 (2015).
40. Pozo, M. & Calvo, J. An overview of authigenic magnesian clays. *Minerals* **8**, 520 (2018).
41. Chase, J. E., Arizaleta, M. L. & Tutolo, B. M. A series of data-driven hypotheses for inferring biogeochemical conditions in alkaline lakes and their deposits based on the behavior of Mg and SiO₂. *Minerals* **11**, 106 (2021).
42. Sawaki, Y. et al. The Ediacaran radiogenic Sr isotope excursion in the Doushantuo Formation in the Three Gorges area, South China. *Precambrian Res.* **176**, 46–64 (2010).
43. Shields, G. & Veizer, J. Precambrian marine carbonate isotope database: Version 1.1: CARBONATE ISOTOPE DATABASE. *Geochim. Geophys. Geosystems* **3**, 1 of 12–12 (2002).
44. Zhao, Y.-Y., Jiang, S.-Y., Li, D. & Yang, J.-H. A petrographic and geochemical study of carbonate and silica phases from the Ediacaran Doushantuo Formation in the Three Gorges area of South China: Implications for diagenetic conditions. *Palaeogeogr. Palaeoclimatol. Palaeoecol.* **463**, 150–167 (2016).
45. Nathan, Y. & Sass, E. Stability relations of apatites and calcium carbonates. *Chem. Geol.* **34**, 103–111 (1981).
46. Rouwet, D., Christenson, B., Tassi, F. & Vandemeulebrouck, J. *Volcanic Lakes*. (Springer, 2015).
47. *Stratigraphy and Paleolimnology of the Green River Formation, Western USA*. vol. 1 (Springer Netherlands, 2015).
48. Deocampo, D. M. Authigenic clay minerals in lacustrine mudstones. in *Geological Society of America Special Papers* vol. 515 49–64 (Geological Society of America, 2015).
49. Raiswell, R. & Canfield, D. E. The iron biogeochemical cycle past and present. *Geochem. Perspect.* **1**, 1–220 (2012).
50. Siever, R. The silica cycle in the Precambrian. *Geochim. Cosmochim. Acta* **56**, 3265–3272 (1992).
51. Xiao, S., Schiffbauer, J. D., McFadden, K. A. & Hunter, J. Petrographic and SIMS pyrite sulfur isotope analyses of Ediacaran chert nodules: Implications for microbial processes in pyrite rim formation, silicification, and exceptional fossil preservation. *Earth Planet. Sci. Lett.* **297**, 481–495 (2010).
52. Hood, A. V. S. & Wallace, M. W. Neoproterozoic marine carbonates and their paleoceanographic significance. *Glob. Planet. Change* **160**, 28–45 (2018).
53. Tosca, N. J., Macdonald, F. A., Strauss, J. V., Johnston, D. T. & Knoll, A. H. Sedimentary talc in Neoproterozoic carbonate successions. *Earth Planet. Sci. Lett.* **306**, 11–22 (2011).
54. Gao, Y. et al. Reconstruction of the Ediacaran sulfur cycle and oceanic redox evolution in shallow-water regions of the Yangtze platform, South China. *Precambrian Res.* **353**, 106004 (2021).
55. Kikumoto, R. et al. Nitrogen isotope chemostratigraphy of the Ediacaran and Early Cambrian platform sequence at Three Gorges, South China. *Gondwana Res.* **25**, 1057–1069 (2014).
56. Halevy, I. & Bachan, A. The geologic history of seawater pH. *Science* **355**, 1069–1071 (2017).
57. Krissansen-Totton, J. & Catling, D. C. A coupled carbon-silicon cycle model over Earth history: reverse weathering as a possible explanation of a warm mid-Proterozoic climate. *Earth Planet. Sci. Lett.* **537**, 116181 (2020).
58. Weaver, C. E. *Clays, muds, and shales*. (Elsevier: Distributors for the U.S. and Canada, Elsevier Science Pub. Co, 1989).
59. Wollast, R., Mackenzie, F. T. & Bricker, O. P. Experimental precipitation and genesis of sepiolite at earth-surface conditions. *Am. Mineral.* **53**, 1645–1662 (1968).
60. Conley, D. J. et al. Biosilicification Drives a Decline of Dissolved Si in the Oceans through Geologic Time. *Front. Mar. Sci.* **4**, (2017).
61. Lazar, B., Starinsky, A., Katz, A., Sass, E. & Ben-Yaakov, S. The carbonate system in hypersaline solutions: Alkalinity and CaCO₃ solubility of evaporated seawater: Carbonate in evaporated seawater. *Limnol. Oceanogr.* **28**, 978–986 (1983).
62. Zhang, S. et al. New paleomagnetic results from the Ediacaran Doushantuo Formation in South China and their paleogeographic implications. *Precambrian Res.* **259**, 130–142 (2015).
63. Brennan, S. T., Lowenstein, T. K. & Horita, J. Seawater chemistry and the advent of biocalcification. *Geology* **32**, 473 (2004).
64. M. A. McCaffrey, B. Lazar, H. D. Ho. The Evaporation Path of Seawater and the Coprecipitation of Br- and K+ with Halite. *SEPM J. Sediment. Res.* **Vol. 57**, (1987).
65. Tréguer, P. J. & De La Rocha, C. L. The world ocean silica cycle. *Annu. Rev. Mar. Sci.* **5**, 477–501 (2013).
66. Baldermann, A., Warr, L. N., Letofsky-Papst, I. & Mavromatis, V. Substantial iron sequestration during green-clay authigenesis in modern deep-sea sediments. *Nat. Geosci.* **8**, 885–889 (2015).
67. Liu, P., Yin, C., Chen, S., Tang, F. & Gao, L. The biostratigraphic succession of acanthomorphic acritarchs of the Ediacaran Doushantuo Formation in the Yangtze Gorges area, South China and its biostratigraphic correlation with Australia. *Precambrian Res.* **225**, 29–43 (2013).
68. Knauth, L. P. Temperature and salinity history of the Precambrian ocean: implications for the course of microbial evolution. *Palaeogeogr. Palaeoclimatol. Palaeoecol.* **219**, 53–69 (2005).
69. Reinhard, C. T. et al. Evolution of the global phosphorus cycle. *Nature* **541**, 386–389 (2017).
70. Cox, G. M., Lyons, T. W., Mitchell, R. N., Hasterok, D. & Gard, M. Linking the rise of atmospheric oxygen to growth in the continental phosphorus inventory. *Earth Planet. Sci. Lett.* **489**, 28–36 (2018).
71. Cook, P. J. & Shergold, J. H. Phosphorus, phosphorites and skeletal evolution at the Precambrian–Cambrian boundary. *Nature* **308**, 231–236 (1984).
72. Muscente, A. D., Hawkins, A. D. & Xiao, S. Fossil preservation through phosphatization and silicification in the Ediacaran Doushantuo Formation (South China): a comparative synthesis. *Palaeogeogr. Palaeoclimatol. Palaeoecol.* **434**, 46–62 (2015).
73. Tarhan, L. G., Hood, A. V. S., Droser, M. L., Gehling, J. G. & Briggs, D. E. G. Exceptional preservation of soft-bodied Ediacara Biota promoted by silica-rich oceans. *Geology* **44**, 951–954 (2016).

74. Laakso, T. A., Sperling, E. A., Johnston, D. T. & Knoll, A. H. Ediacaran reorganization of the marine phosphorus cycle. *Proc. Natl. Acad. Sci.* **117**, 11961–11967 (2020).
75. Millero, F. J., Feistel, R., Wright, D. G. & McDougall, T. J. The composition of Standard Seawater and the definition of the Reference-Composition Salinity Scale. *Deep Sea Res. Part Oceanogr. Res. Pap.* **55**, 50–72 (2008).
76. Parkhurst, D. L. & Appelo, C. A. J. *Description of Input and Examples for PHREEQC Version 3—A Computer Program for Speciation, Batch-Reaction, One-Dimensional Transport, and Inverse Geochemical Calculations.* (2013).
77. Voigt, M., Marieni, C., Clark, D. E., Gislason, S. R. & Oelkers, E. H. Evaluation and refinement of thermodynamic databases for mineral carbonation. *Energy Procedia* **146**, 81–91 (2018).
78. Catalano, J. G. Thermodynamic and mass balance constraints on iron-bearing phyllosilicate formation and alteration pathways on early Mars. *J. Geophys. Res. Planets* **118**, 2124–2136 (2013).
79. Datasets of 'Authigenic clay mineral evidence for restricted, evaporitic conditions during the emergence of the Ediacaran Doushantuo Biota'. <https://doi.org/10.6084/m9.figshare.19919321.v2> (2022).

Acknowledgements

This work was conducted at Macquarie University while S. Han was a cotutelle student of China University of Geosciences Beijing and Macquarie University, funded by China Scholarship Council (No. 201906400045). We thank M. Kennedy for inspiring this work, Z. Shen and Y. Wu for fieldwork assistance, S. Murray, P. Wieland, T. Murphy, and C. Wheeler for assistance in the lab and M. Rafiei, B. Teece, C. Bai and G. Shields for helpful discussions.

Author contributions

Conceptualization: S.C.L., B.Y., S.H. Methodology: S.C.L., A.B., M.V. Investigation: S.H., S.C.L. Visualization: S.H., M.V. Supervision: S.C.L., B.Y., A.A. Writing—original draft: S.H. Writing—review & editing: S.C.L., A.A., A.B., B.Y., S.H., M.V.

Competing interests

The authors declare no competing interests.

Additional information

Supplementary information The online version contains supplementary material available at <https://doi.org/10.1038/s43247-022-00495-6>.

Correspondence and requests for materials should be addressed to Shujun Han.

Peer review information *Communications Earth & Environment* thanks Zhao Yanyan, Thomas Bristow and Ganqing Jiang for their contribution to the peer review of this work. Primary Handling Editor: Joe Aslin.

Reprints and permission information is available at <http://www.nature.com/reprints>

Publisher's note Springer Nature remains neutral with regard to jurisdictional claims in published maps and institutional affiliations.



Open Access This article is licensed under a Creative Commons Attribution 4.0 International License, which permits use, sharing, adaptation, distribution and reproduction in any medium or format, as long as you give appropriate credit to the original author(s) and the source, provide a link to the Creative Commons license, and indicate if changes were made. The images or other third party material in this article are included in the article's Creative Commons license, unless indicated otherwise in a credit line to the material. If material is not included in the article's Creative Commons license and your intended use is not permitted by statutory regulation or exceeds the permitted use, you will need to obtain permission directly from the copyright holder. To view a copy of this license, visit <http://creativecommons.org/licenses/by/4.0/>.

© The Author(s) 2022